



Synthesis of Copper–Nickel and Iron–Nickel Alloys by Hydrogen Reduction of Mixtures of Metal Oxide Powders

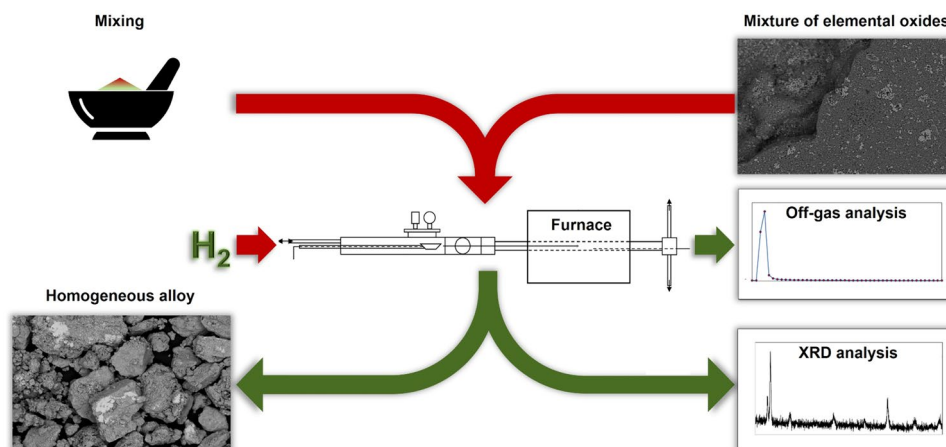
Arun Kamalasekaran¹ · Pelle Mellin² · Christopher Hulme¹

Received: 1 April 2024 / Accepted: 4 July 2024 / Published online: 17 July 2024
© The Author(s) 2024

Abstract

The vast majority of metals production is based on the use of carbon as a reductant and/or a heating fuel. This results in a large amount of carbon dioxide emissions and should be minimized to limit global warming. In this study, powders of copper–nickel alloy and iron–nickel of varying compositions were produced in a single step by reduction of mixtures of Cu_2O -NiO and Fe_2O_3 -NiO powders, respectively, using hydrogen as a reductant. Reduction was performed in a horizontal tube furnace at 700 °C for 45 min. All processing was in the solid state and alloys were produced directly from elemental metal oxides. Exhaust gases were analyzed using a gas analyzer to measure the water content to track the progress of the reduction. Reduction was declared complete when the water content in exhaust gases matched the level before hydrogen was introduced. Both copper–nickel and iron–nickel alloys were produced successfully. X-ray diffractometry confirmed the absence of oxides in the product and the presence of solid phases in agreement with the relevant binary phase diagram. Energy-dispersive X-ray spectroscopy in a scanning electron microscope showed macroscopic homogeneity at the expected composition for each powder mixture directly after reduction, with microscopic fluctuations of the order of several mass percent, within the limits of fluctuations observed following typical casting processes. These promising results warrant further investigation to apply this concept to more chemistries and to scale up the process to a pilot scale.

Graphical Abstract



Keywords Hydrogen reduction · Solid-state reduction · Kinetics · Iron–nickel · Copper–nickel · Material characterization

The contributing editor for this article was Xue Feng Dong.

Extended author information available on the last page of the article

Introduction

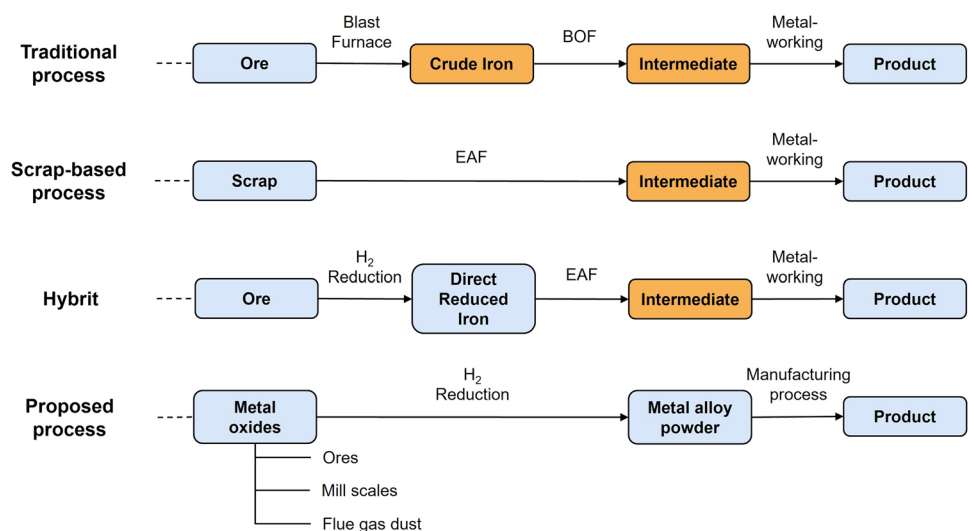
In recent years, there has been much activity concerning the replacement of carbon-based reductants in iron making. This is due to the high amount of carbon dioxide emitted by the iron and steel industries: in 2019, the global emission by this sector accounted for 2.6 Gt of carbon dioxide and this represents one-quarter of the carbon dioxide emitted by all industries. Around 5% of the carbon dioxide emissions in the EU region and 7% globally come from steel industries and this value is high for a single sector of the economy [1, 2]. However, the iron and steel sector cannot be completely replaced as it makes a huge contribution to the global economy and is vital to ensure continued economic development and to increase the standard of living in developing countries. The total value-added contribution by the steel industry in the year 2017 accounted for US\$2.9 trillion, which is 3.8% of the global GDP [3]. Therefore, it is necessary to change the practices in this sector to use alternative processes that do not emit large quantities of carbon dioxide. Scrap-based processing has a role to play in this transition, although the limited availability of scrap and declining scrap quality means that the industry must continue to produce virgin material by reduction of ores. One technology that is investigated widely is the substitution of fossil carbon as a reductant by either biocarbon or hydrogen. In the case of biocarbon, it can be used as a replacement for pulverized coal injection in blast furnaces, or it can be gasified to produce syngas and used as a reductant of ores in a solid-state reaction to give a so-called direct reduction technique [4]. Hydrogen is also used in this way. In the 2020 technology road map devised by the International Energy Agency, it is stated that the utilization of green hydrogen as a primary

reducing agent in the iron and steel sector is expected to reach a commercial scale by mid-2030s. Furthermore, green hydrogen and carbon capture, utilization and storage can cumulatively reduce emissions in the Sustainable Development Scenario by one-quarter [1, 5]. This scenario depicted in the 2020 technology road map can also be realized by looking at the key hydrogen reduction technology projects such as Hybrit (SSAB, LKAB and Vattenfall, Sweden), GreenIron, H2 Green Steel, and Hamburg pilot project (ArcelorMittal, Germany) [5].

Since pyrometallurgical research overwhelmingly concentrates on the replacement of carbon-based reductants in iron making, most notably replacing the blast furnace, the aim of the research work in this article is to replace or avoid the downstream processes needed to produce alloys, while also replacing carbon-based reductants with hydrogen. The ultimate goal is to produce any arbitrary alloy directly from suitable mixtures of oxides. This could be alloys in the final compositions of products using a new production route (Fig. 1); alternatively, hydrogen-based reduction could produce carbon- and energy-intensive precursor materials, such as ferroalloys, used in existing processes in the steel industry. Both applications shall be explored in this study and future-related work.

The current study aims to understand the fundamental materials science behind producing any metal alloy by hydrogen reduction of their respective metal oxide powders in solid state. As a proof of concept, it is preferable to select a simple binary alloy system with oxides that exhibit relatively low stability, that are inexpensive, that have some direct industrial applications, and that avoid major chemical hazards. Based on these criteria, the iron–nickel (also known as the ferronickel) system is a strong candidate; however, the iron–nickel system has the potential to form intermetallics such as FeNi_3 , which may influence the reduction and

Fig. 1 Comparison of proposed process with traditional, scrap-based, and Hybrit processes. Reddish-orange blocks show process steps that involve melting the input material (Color figure online)



homogenization processes, even though it is metastable in nature and its formation is kinetically limited above 500 °C [6]. Such effects may include providing a low-energy route for reduction, or forming intermediates that hinder overall reduction or homogenization kinetics. For this reason, copper–nickel, which has less industrial relevance but avoids the formation of any intermetallics, was also selected for the proof-of-concept study [7].

Around 0.3 Gt of carbon dioxide (of the total of 2.6 Gt of carbon dioxide emitted from iron and steel sector) is emitted due to the usage of lime fluxes and other steps in the production of such ferroalloys [1]. Nickel alone contributes to 23.8% of carbon dioxide emissions of the stainless steel industry, and the production of iron–nickel alloy (35% Ni) and nickel pig iron (10% Ni) that are used in stainless steel making emits 6 tCO₂-equivalent/t alloy and 7 tCO₂-equivalent/t alloy, respectively. The major contribution to greenhouse gas emission comes from the usage of carbon-based reductants and fossil fuels [8]. Even though the overall aim of current study is to provide a proof of concept for general alloy production and not to provide a new production route for iron–nickel alloys specifically, this shows an example of the potential of the proposed technique to reduce carbon dioxide emissions and energy consumption. The application of iron–nickel alloys is not restricted to steel production. Iron–nickel alloys are used in magnetics (Fe–50Ni) and from the late 1970s, they have been considered as a potential candidate to replace cobalt-based binders used in cemented carbide tools. Cobalt is a critical raw material and supply is heavily dependent on the Democratic Republic of the Congo, which is often in a state of civil unrest or war [9, 10]. From the late 1990s, cemented carbide tools produced with iron- and nickel-based binder systems have been used commercially in woodworking and production of special wear parts [11–13]. The iron–nickel alloy powders used as alternative binders are produced using water and gas atomization, where the pre-alloyed iron–nickel alloy is melted and broken into droplets using fast-moving fluid. This is energy-intensive. An alternative method of producing iron–nickel alloy powder mixtures is mixing iron and nickel powder through admixing or by chemical or diffusion-bonding processes [13]. However, no new approach has yet succeeded in displacing cobalt-based binders and improving the sustainability of cemented carbide tools.

The steps involved in the reduction of Fe₂O₃ in the ferric and nickel oxides powder mixture using hydrogen at temperatures above 570 °C are as follows: reduction of Fe₂O₃ to Fe₃O₄, followed by formation of FeO from Fe₃O₄ and finally, reduction of FeO to metallic iron [14]. On the other hand, the NiO in the oxides powder mixture directly reduces to metallic nickel. NiO is less thermodynamically stable with respect to its elements in their standard states than FeO and so it requires less energy to reduce [15]. This implies that the

reduction of NiO in the mixture would be complete before that of FeO. The Baur–Glässner diagram for Fe–O–H₂ shows that higher reduction temperatures are favorable, since both iron and FeO are stable over a wider range of conditions as temperature increases [16].

Materials

As an initial trial, 50 wt% cuprous oxide (Cu₂O, Alfa Aesar—ThermoFisher GmbH, Kandel, Germany; country of origin: United States of America; particles ≤ 23 μm; > 99.9% purity) was mixed with 50 wt% nickel oxide (NiO, Sigma Aldrich Chemie GmbH, Steinheim am Albuch, Germany; country of origin: China; particles 44 μm; > 99% purity) manually using a mortar and pestle for 5 min to produce 1 g of mixed powder. At the end of every minute, the mixing was stopped, and the powders that had spread out were collected using a spatula before restarting the mixing process. The mixing time was kept short as to prevent mechanical alloying of the oxide powders. From the 1 g mixture, 0.10 g was used in each reduction trial. With equal masses of both oxides, it is expected from the atomic masses of each element that the proportion of metal atoms that are nickel is 47 wt%, and so the reduced alloy is expected to have the overall composition Cu–47 wt% Ni.

Fe–Ni alloy powders with varying composition of Fe and Ni, were produced using the same procedure as the Cu–Ni alloy. Ferric oxide (Fe₂O₃, Sigma Aldrich Chemie GMBH, Steinheim am Albuch Germany, country of origin: China, < 5 μm, > 96% purity) and NiO powders (as above) were mixed in various proportions to achieve different final alloys, as listed in Table 1. Furthermore, Fig. 2 shows the morphology of the Cu₂O, Fe₂O₃ and NiO powders (precursors) used to produce the mixtures mentioned in this section.

Experimental Methods

The experimental setup consists of a gas inlet for gases such as argon and hydrogen, a plug valve to switch between the gas connection and the vacuum pump, an overpressure valve and a pressure gauge, and a push rod connected to a crucible containing the raw material (Fig. 3). The horizontal quartz tube in the furnace is isolated from the inlet chamber

Table 1 Compositions (wt%) of mixtures of Fe₂O₃ and NiO for alloy production

Raw material sample	1	2	3	4	5
Fe ₂ O ₃	80	60	50	40	18

The residue of the sample is NiO

Fig. 2 Secondary electron images of the precursors: **a** Cu_2O , **b** Fe_2O_3 and **c** NiO

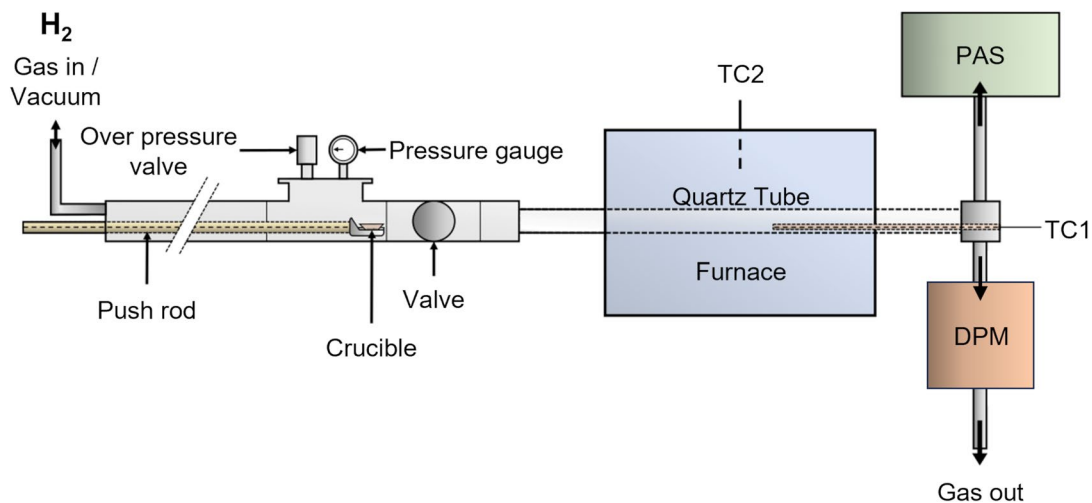
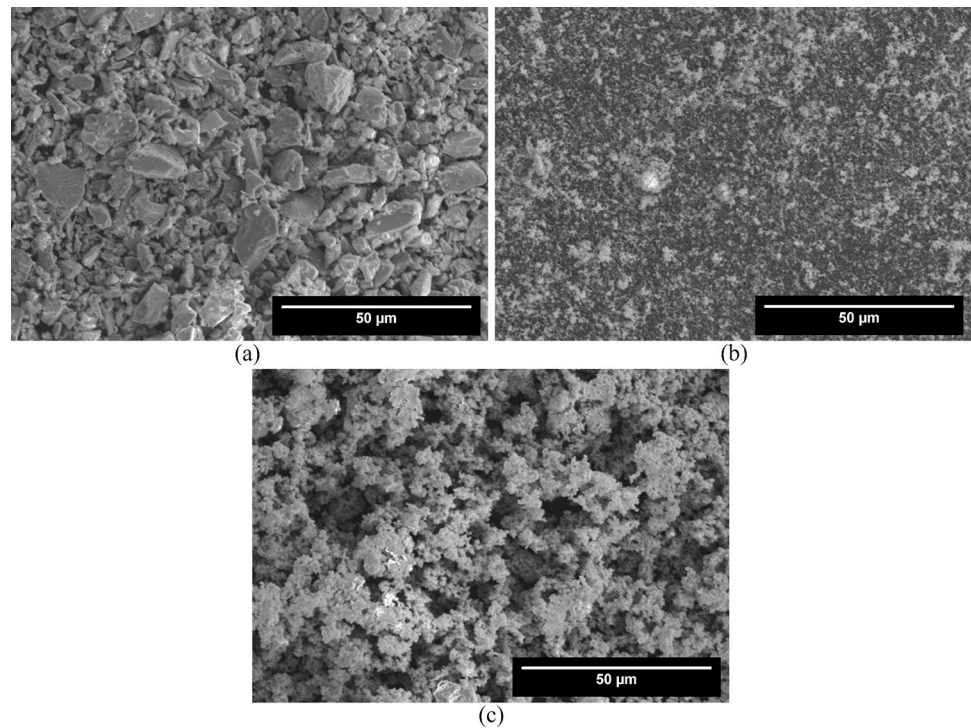


Fig. 3 Experimental setup containing horizontal quartz tube furnace with a push rod mechanism to handle the sample, thermocouples (TC), a gas inlet, and a gas outlet connected to a photoacoustic multi-gas monitor (PAS) and a dew point meter (DPM)

using a ball valve, during vacuum pumping and raw material charging operations. Thermocouple 1 (TC1) provides the temperature of the hot zone where the sample is placed; the temperature near the wall of the quartz tube is recorded using thermocouple 2 (TC2). The outlet of the quartz tube is divided and off-gas flows to a photoacoustic multi-gas monitor and a dew point meter simultaneously. The dew point meter measures moisture content in parts per million by volume; the photoacoustic multi-gas monitor analyzes

the gas composition and moisture content (in parts per million by volume) of the off-gas at one-minute intervals. As the dew point meter is calibrated for argon as a carrier gas, its data are considered to be strictly qualitative when other gases make up the majority of the experimental atmosphere, as in the current study, where hydrogen is the main component of the exhaust gas mixture. The photoacoustic multi-gas monitor is calibrated for hydrogen atmosphere and is, therefore, considered the main source of data to track the

reduction process in the current study. From the 1 g sample of each oxide mixture, 0.10 g was used in each reduction trial, in order to not to exceed the moisture content limit of the photoacoustic multi-gas monitor (ca. 14,000 ppm).

In each experiment, the crucible was placed at one end of the push rod and the lid was tightly fastened to make the environment gas-tight. The air in the inlet chamber was then removed using the vacuum pump and the chamber was then filled with argon at 1 Nl min⁻¹ before heating. The photoacoustic multi-gas monitor was turned off to avoid the accumulation of water from the environment, which could saturate the detector. In initial trials, three different temperatures: 425 °C, 562 °C and 700 °C were used for isothermal reduction of separate samples of the Cu₂O-NiO mixture. The minimum reduction temperature (425 °C) was obtained from literature, even though the composition of Cu₂O-NiO mixture used in the current study is different from the published data [17]. When the water concentration in the off-gas was below 100 ppm according to the dew point meter (which is the appropriate tool, since at this point in the trial the atmosphere is predominantly argon), hydrogen was introduced at a flow rate of 0.6 Nl min⁻¹. The photoacoustic multi-gas monitor was then turned on and the crucible with the sample was pushed into the hot zone of the quartz tube furnace. All samples were exposed to the hydrogen atmosphere for a fixed time of 45 min, based on the experience of the furnace operator. A peak in the water concentration was observed immediately after the sample was introduced to the hot zone, before slowly returning to its initial level. The rise of moisture content to the maximum level and its drop to the initial level happened within the 45 min fixed reduction time. The trial was terminated after the moisture content in the off-gas returned to the level at the start of the trial, implying that no water was being generated from the sample, and the sample was cooled under argon inside the quartz tube but outside the hot zone of the furnace. The temperature at the hot zone and near the furnace wall was continually recorded during the trial. The argon supply was stopped when the reduced product (Cu-Ni alloy powder) in the crucible was observed to have reached ambient temperature, after which the furnace lid was opened. The product was removed and was immediately stored in an airtight package. The airtight package was then stored in a vacuum desiccator.

The same experimental procedure was used to produce all Fe-Ni alloy powders. Five 0.10 g samples, obtained from different raw material mixtures, designated RM_x, where 1 ≤ *x* ≤ 5, were reduced isothermally at 700 °C using hydrogen gas with a flow rate of 0.6 Nl min⁻¹, to produce Fe-Ni alloys, designated FN_x, where 1 ≤ *x* ≤ 5. In both these cases, the value of *x* indicates the raw material mixture from which each alloy was produced. These designations have been extensively used in the RESULTS AND DISCUSSION section. Furthermore, the reduction temperature was

fixed at 700 °C, based on the results in existing literature [16, 18–21]. This reduction temperature was also tried in the reduction of pure Fe₂O₃, Fe₃O₄, FeO and NiO powders individually before using it for the reduction trials involving the raw materials mixtures. The reduction time for all the trials was 45 min, as for the Cu-Ni trials and the reduction of all the oxide powder mixtures was observed to be complete within this time.

Calculation of Total Oxygen Content in Off-Gas

For all the Cu-Ni and Fe-Ni experimental trials, curves were fitted to the water concentration data using the Cauchy distribution (Eq. 1) [22].

$$k \left[1 + \left(\frac{x-a}{b} \right)^2 \right]^{-1} \quad (1)$$

where *a* and *b* are fitting variables and *k* is a constant that has been used to normalize the density function so that it integrates to 1.

In this curve fitting method, different combinations of variables and normalizing constants were identified and optimized using the Solver tool in Microsoft Excel (Version 2402). The combination of variables which gave the lowest value in a chi-square value was chosen. The function was then integrated between time limits at which the water concentration levels correspond to the base level. The area under curve (total water content) obtained through integration was used to calculate total oxygen loss that occurred during effective reduction time of each trial. The total oxygen loss was then compared with estimated oxygen content in the respective raw material, to confirm the completion of the reduction process and to test the reliability of the measurements. In all the calculations, the minimum amount of raw material mixture was considered to be 0.10 g and the maximum amount to be 0.12 g, as these limits were the acceptance criteria while weighing the raw material before all reduction trials.

Characterization

X-ray diffractometry (XRD) analysis was performed using a Siemens D5000 diffractometer with a copper source. The XRD instrument was operated in the traditional Bragg–Brentano geometry to confirm the absence of oxides and to identify the phases present in the reduced products. In the XRD analysis of the Cu-Ni alloys, a nickel filter was used to reduce the intensity of the copper Kβ line. In the XRD analysis of the FN_x alloys, the nickel filter was removed, and a graphite monochromator was used instead to avoid fluorescence from the iron atoms.

SEM analyses of the raw materials and reduction products were performed using a Hitachi S-3700N instrument. Energy-dispersive X-ray spectroscopy (EDX) of the samples was performed with an accelerating voltage of 15 kV. The X-ray spectra from different regions in the sample were analyzed through EDX mapping, point, area, and line analysis, using the software ESPRIT v.19.1. The morphology of the samples was studied using this same instrument in secondary electron and backscatter electron modes.

Results and Discussion

Cu-Ni Alloy

Three isothermal reduction trials were performed at three different temperatures: 425 °C, 562 °C, and 700 °C. These trials were used for validating the experimental setup. In all these trials, the water concentration in the off-gas was measured using the photoacoustic multi-gas (PAS) monitor,

just before pushing the oxide powder mixture into the hot zone (Fig. 4). The water concentration was observed to be 78 ppm, 77 ppm, and 99 ppm, respectively, at the beginning of all three Cu-Ni trials. These trials were performed for 45 min, and the water concentration in the off-gas was observed to peak within a few minutes after introducing the oxide powder mixture into the hot zone, after which it gradually decreased back to the initial value after approximately 30 min and certainly well within the 45 min experimental time. This suggests that the oxygen in the oxide powder mixture has been removed and, hence, that the reduction process is complete. The peak values are observed to descend with increase in temperature and this has to do with the frequency at which the H₂O concentration data was collected by the PAS monitor. Data were collected every minute, and there is a possibility that the actual peak caused by a more spontaneous release of H₂O at 700 °C, compared to 425 °C and 562 °C, was not captured.

Figure 5 shows a curve plotted using the probability distribution function for the Cauchy distribution and Eq. 2 its

Fig. 4 Water concentration in the off-gas emitted during the production of Cu-47 wt% Ni alloy at different reduction temperatures: 425 °C, 562 °C, and 700 °C

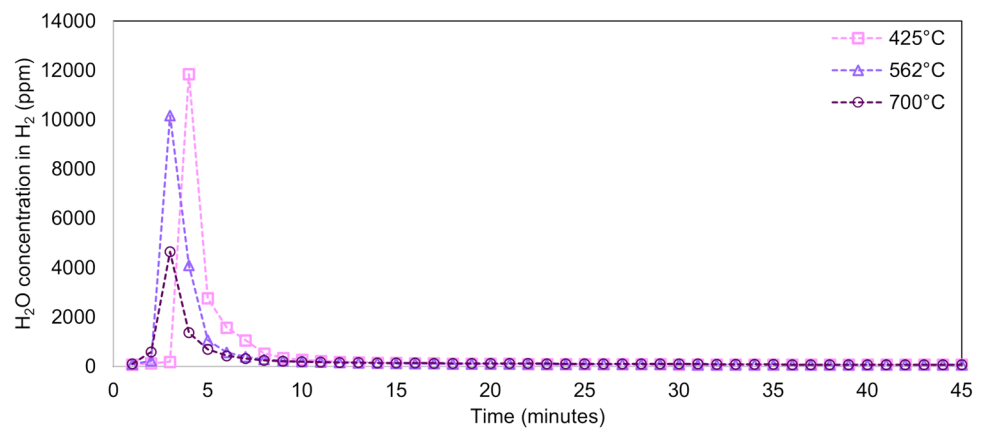
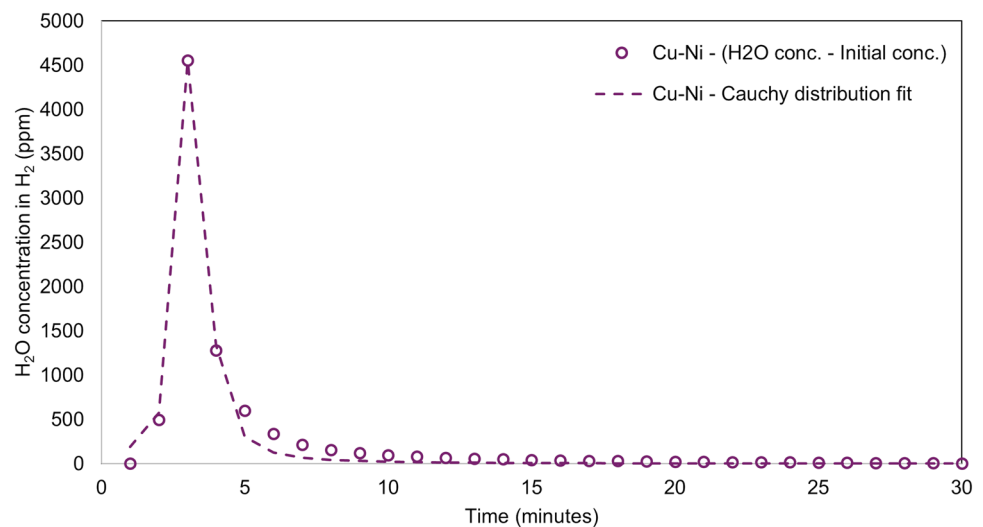


Fig. 5 Total water content in the off-gas emitted during the production of Cu-47 wt% Ni alloy at the reduction temperature 700 °C



function. The summation of chi-square values for the H₂O concentrations calculated using the variate and constant combination shown in Eq. 2 was observed to be the lowest compared to other combinations. Therefore, the curve generated using Eq. 2 is a good fit. Area under the curve was determined by definite integration of the curve function, and this area represents the total amount of water emitted from the beginning of reduction process and until the time when the water concentration reached the initial concentration (99 ppm). In the Cu-Ni isothermal reduction trial performed at 700 °C, it can be calculated from the area under the curve that the off-gas contained 24 mg of oxygen. 0.10 g of Cu₂O—50 wt% NiO (raw material) contains 16 mg of oxygen, and 0.12 g of the same raw material contains 20 mg of oxygen. Since the total oxygen content in

the off-gas is higher than the total oxygen content in the raw material prior reduction, and the difference between them is small, the reduction process can thus be declared complete and the measurements are consistent with expectations.

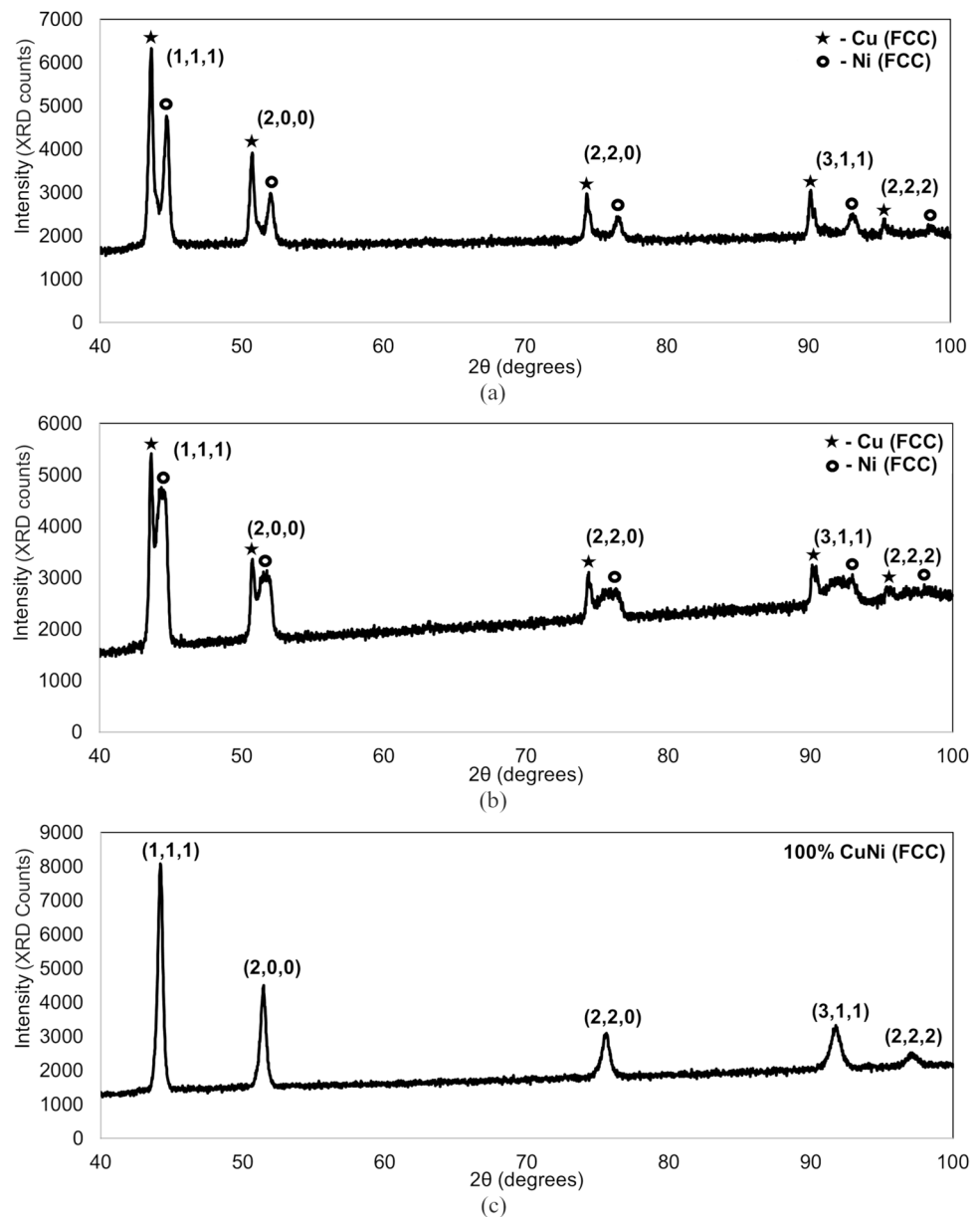
The curve function is,

$$f(t) = \left[\frac{6257.12}{1 + \left(\frac{t-3.24}{0.40} \right)^2} \right] \quad (2)$$

where t is reduction time in minutes.

X-ray diffractograms (Fig. 6) of the samples following reduction supported the conclusion that all oxygen had been

Fig. 6 X-ray diffractograms of Cu-47 wt% Ni produced at different reduction temperatures: **a** 425 °C, **b** 562 °C, and **c** 700 °C



removed from the sample, as the peaks present no longer correspond with the oxides added in the mixture, but to face-centered cubic crystals with lattice parameters typical of copper–nickel alloys. This is in accordance with the copper–nickel equilibrium phase diagram [23]. The alloys obtained from trials run at 425 °C and 562 °C generated two separate families of peaks that each followed the systematic absences attributed to a face-centered cubic crystal, and lattice parameters (3.608 ± 0.001 Å and 3.522 ± 0.001 Å, respectively), which are very close to those of pure copper and pure nickel [24, 25]. In contrast, the alloy produced at 700 °C generated a single set of sharp peaks consistent with a face-centered cubic crystal with a lattice parameter

of (3.555 ± 0.001) Å, typical of a near-equiatomic copper–nickel alloy [26]. The copper and nickel FCC peaks measured following reduction at 425 °C are sharper and more distinct from each other, compared to those observed following reduction at 562 °C. These results suggest that at the lowest temperature, copper and nickel remained mostly confined to the particles in which they began, either Cu_2O or NiO , and remained as separate phases. Conversely, at the highest temperature tested, the two types of atoms interdiffused extensively to create a single phase. The intermediate temperature resulted in intermediate behavior, with two distinct phases, but a more similar chemistry and broader peaks, suggesting a partial homogenization had occurred.

Scanning electron microscopy and energy-dispersive X-ray spectroscopy were performed on three separate regions of the sample reduced at 700 °C. Figure 7 shows the powder after reduction at 700 °C. Notably, the particles are significantly larger than both the precursor powders (Fig. 2), suggesting that the original oxide particles are no longer distinct and have sintered together to form new particles. The spongy nature of the particles is consistent with similar solid–gas reduction reactions [27–29]. The EDX data showed that the average composition of Cu-47 wt% Ni was found in all three regions of the sample, although there were fluctuations in the composition from one point to another within the regions (Fig. 8). The mean composition was found to be 57 ± 2 wt% copper in all three regions tested, with the most copper rich point exhibiting 90 ± 17 wt% copper and the most nickel-rich at 32 ± 17 wt% copper. The slight discrepancy in composition could be explained easily by slight measurement or mixing errors during sample

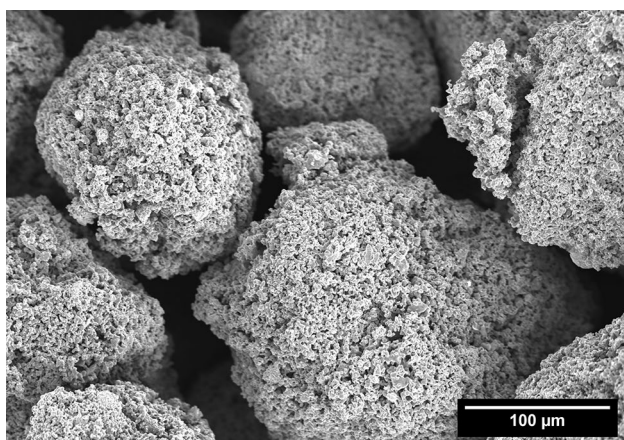
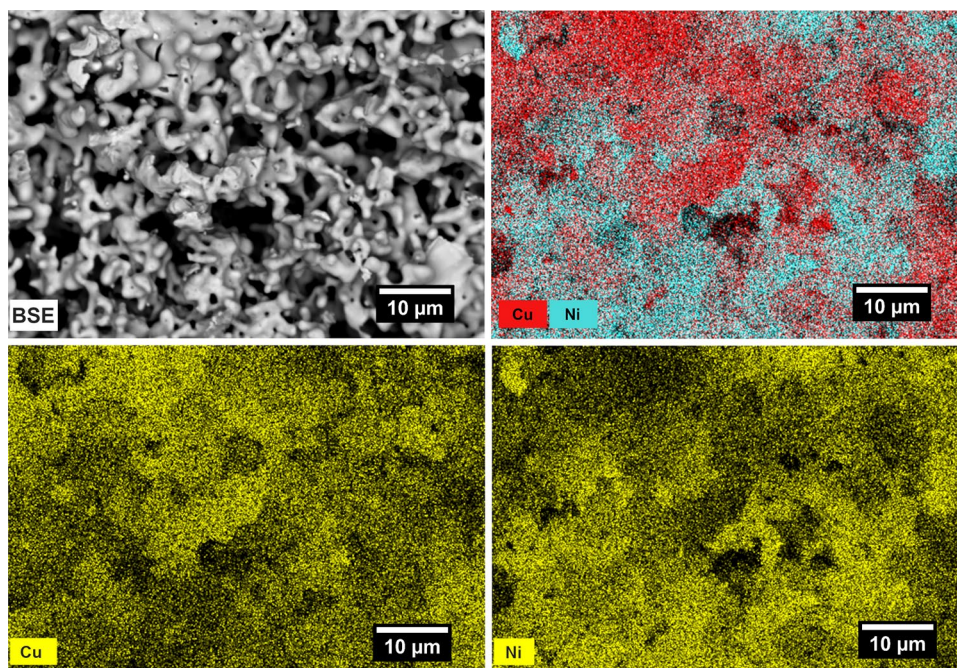


Fig. 7 Secondary electron image of the Cu-47 wt% Ni alloy produced at 700 °C

Fig. 8 Backscattered electron image and energy-dispersive X-ray spectroscopy mapping of Cu-47 wt% Ni alloy produced at 700 °C



preparation: the small sample mass makes the overall composition extremely sensitive to small variations in weighing or incomplete mixing. The large variation in composition from one point to another is unsurprising given the short heating time, the fact that each of the precursor materials only contained one type of metal atom, meaning that the copper and nickel atoms were entirely segregated at the start of the process. Each EDX measurement point is an average over a volume of the order of 1 μm in each direction, and so could easily detect compositional data from within a region that contained only one type of metal atom at the start of the process. The X-ray diffractometry data can be understood as peaks centered on the position with the lattice parameter of the average composition, but with peak broadening caused by the inhomogeneities and associated small variations in local lattice parameter. Since the initial goal of using the experimental setup was to achieve complete reduction of the oxide powders mixture to produce a binary metal alloy, the concept has been proven. While the mean composition was clearly within experimental error of that expected, the alloy was not chemically homogeneous on a microscopic scale. However, the alloy was chemically homogeneous on a macroscopic scale, and it is likely that an additional homogenization step, or a longer hold time at the elevated temperature, is needed to achieve a more homogeneous alloy.

Fe-Ni Alloys

Using the same procedure as for the copper–nickel alloys, a series of iron–nickel alloys, pure iron, and pure nickel were produced separately by isothermally reducing appropriate mixtures of Fe_2O_3 and NiO powders using hydrogen gas at 700 °C (Table 2). Similar to the trials using the copper–nickel alloy, the water concentration in the off-gas peaked within a few minutes after the initiation of the trials and it declined to the initial level after approximately ten minutes of reduction, and well within the set trial time of 45 min (Fig. 9).

Figure 10 and Table 3 show total water content in the off-gas emitted during the production of the Fe-Ni alloys and the total oxygen content calculated from it. The total oxygen content removed from the raw material in all the Fe-Ni trials is higher than the total oxygen content present in the raw material prior to reduction. In the trials involving production of FN1, FN2, and FN4 alloys, the difference between

these two values is small. In the other trials, the difference is large, and this could have happened due to the emission of moisture from the furnace or a leak of ambient air into the furnace during the reduction. However, this does not affect the conclusion that reduction was complete after these two trials as the water concentration declined to its initial level within the set trial time.

All samples were subjected to X-ray diffraction analysis (Fig. 11). In all cases, no peaks consistent with metal oxides were observed, which implies that the reduction was complete. Alloy FN1 contained γ (FCC) and α (BCC) phases. X-ray diffractograms of the rest of the FN x alloys show the presence of a single γ (FCC) phase. These X-ray diffraction results are in accordance with the iron–nickel equilibrium phase diagram [30]. However, the presence of γ (FCC) and α (BCC) phases in FN1 and a single γ (FCC) phase in FN5 does not agree with previously published results, in which an intermetallic, FeNi_3 , was identified [18]. A major difference in the current study is that the samples are cooled rapidly from the reduction temperature to room temperature. This could suppress the formation of low-temperature phases, such as FeNi_3 ; in the previously published work, samples were allowed to cool slowly, giving sufficient time for low-temperature, lower-symmetry phases, including FeNi_3 , to form by diffusional rearrangement of atoms. The presence of single γ (FCC) phase in FN2 and FN3 alloys confirms that they were cooled at a faster rate, similar to FN1 and FN5. Slow cooling would have instead resulted in the formation of FeNi_3 phase in the FN2 and FN3 alloys. This could be investigated by altering the sample cooling rate, but that is beyond the scope of the current study.

FN1, FN3, and FN5 were subjected to SEM analysis to study their morphology (Fig. 12) and check if the targeted composition is homogeneously present throughout the sample (Fig. 13). As with the copper–nickel samples, the product particles are much larger than the precursor particles (Fig. 2). EDX showed that the respective targeted compositions, Fe-22 wt% Ni in the case of FN1 and Fe-84 wt% Ni for FN5, in some areas of the sample and iron- and nickel-rich areas outside these regions, but never pure iron or pure nickel. From Fig. 13 and Table 4, it can be understood that homogenization was ongoing at the end of the heating time, and a longer heating time, or separate homogenization treatment, is needed to achieve a completely even composition on the meso- and microscopic scale.

Table 2 Summary of materials, expected iron content and background off-gas water content for reduction trials in the iron–nickel system

Alloy designation	Iron	FN1	FN2	FN3	FN4	FN5	Nickel
Raw material designation	Fe_2O_3	RM1	RM2	RM3	RM4	RM5	NiO
Fe_2O_3 content/wt%	100	80	60	50	40	18	0
Expected Fe content in the reduced product/wt%	100	78	57	47	37	16	0
Background water concentration in off-gas/ppm	87	124	91	77	92	68	87

Fig. 9 Water concentration in the off-gas emitted during the production of: **a** Fe and Ni powders and **b** Fe-Ni alloys: FN1, FN2, FN3, FN4, and FN5

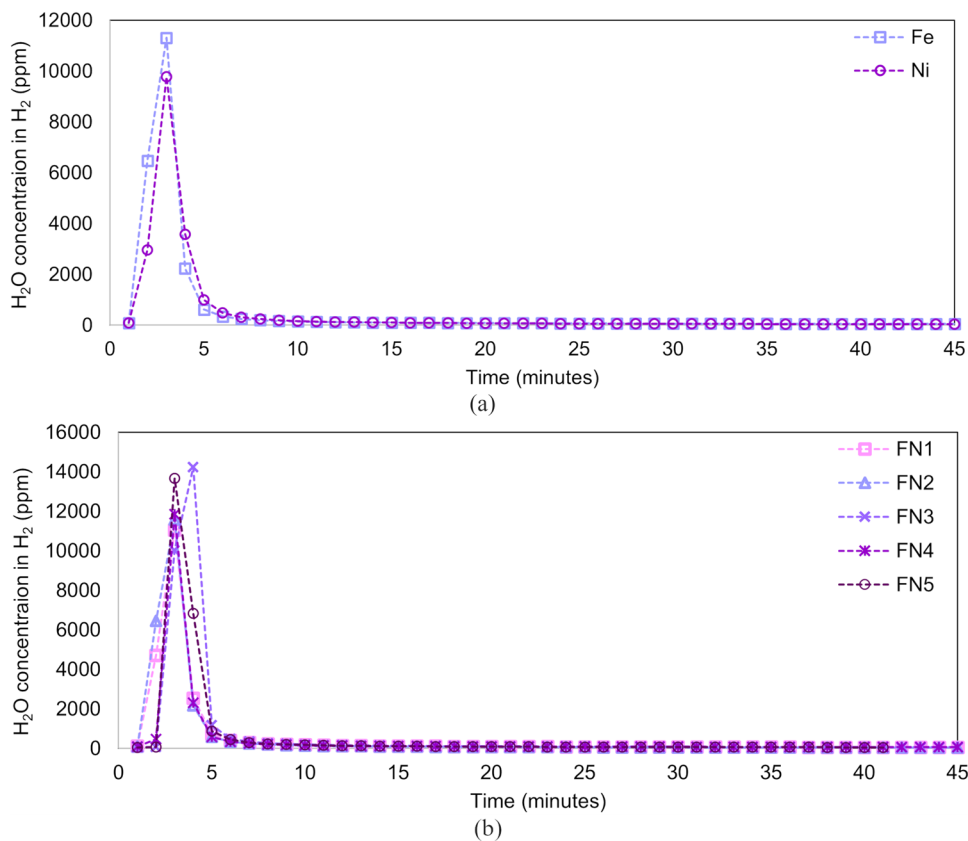
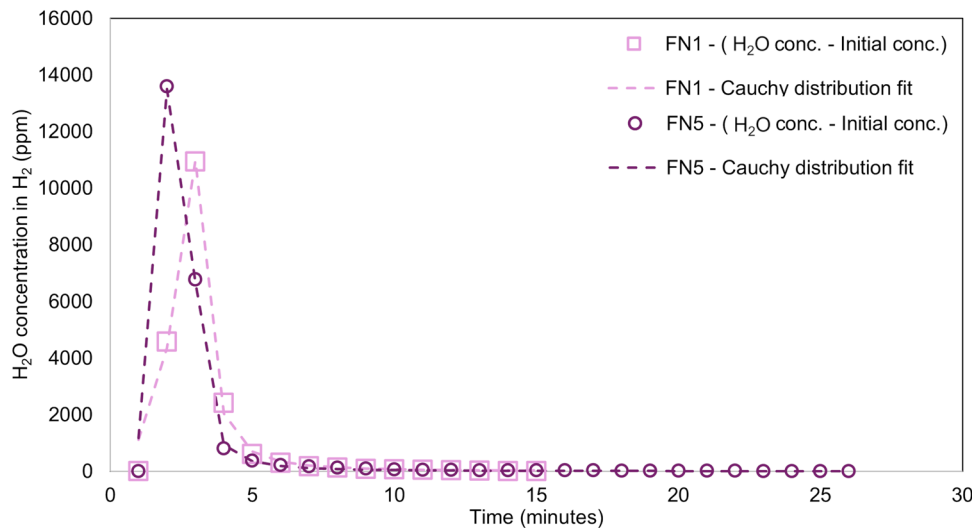


Fig. 10 Total water content in the off-gas emitted during the production of Fe-Ni alloys, FN1 and FN5



Conclusion

Samples consisting of mixtures of iron oxide, nickel oxide, and copper oxide powders were produced and subjected to a hydrogen atmosphere at elevated temperature for an extended time. In all cases, oxygen was eliminated from

the material and a metal alloy was formed. The main conclusions of this study are as follows:

- It is feasible to form Cu-Ni and Fe-Ni alloys directly from mixtures of pure oxide powders using hydrogen as a gaseous reducing agent on a laboratory scale.

Table 3 Total oxygen content in the off-gas emitted during the production of Fe-Ni alloys, and its comparison with the expected oxygen content in off-gas

Alloy designation	FN1	FN2	FN3	FN4	FN5
Total H ₂ O concentration in off-gas/ $\mu\text{l/l}$ (Area under curve)	19,743	26,916	157,259	31,080	119,323
Total H ₂ O in off-gas/mg	40	50	651	83	414
Total O ₂ in off-gas/mg	35	45	579	74	368
Minimum expected O ₂ content in off-gas/mg (0.10 g raw material)	28	27	26	25	23
Maximum expected O ₂ content in off-gas/mg (0.12 g raw material)	34	32	31	30	28

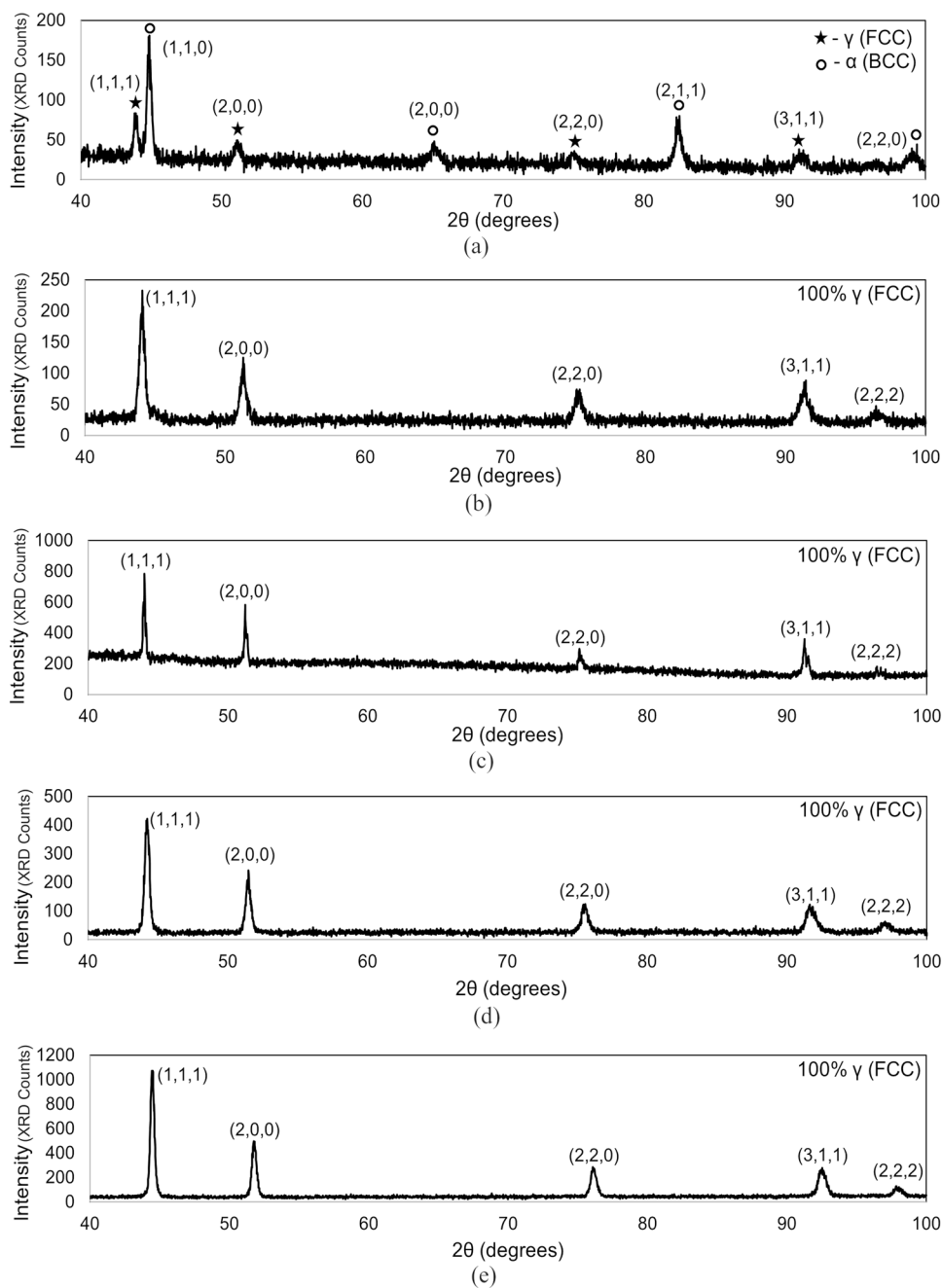
Fig. 11 X-ray diffractograms of Fe-Ni alloys: **a** FN1, **b** FN2, **c** FN3, **d** FN4 and **e** FN5

Fig. 12 Secondary electron images of: **a** Fe-22 wt% Ni (FN1) alloy and **b** Fe-84 wt% Ni (FN5) alloy

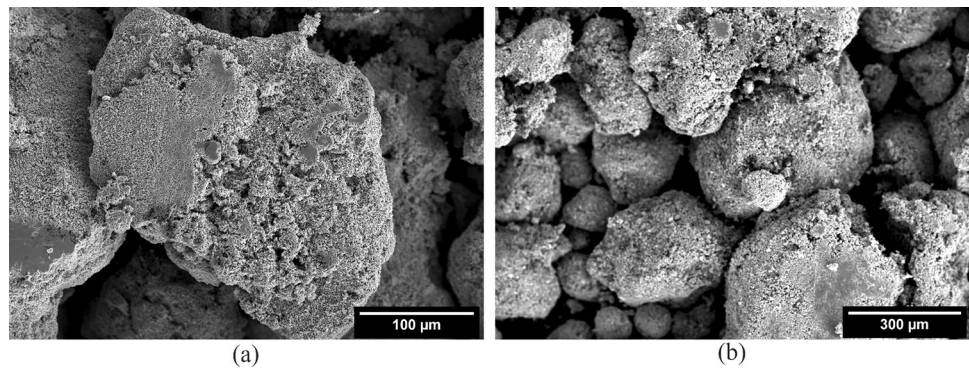


Fig. 13 Backscattered electron image and energy-dispersive X-ray spectroscopy mapping of Fe-53 wt% Ni alloy (FN3)

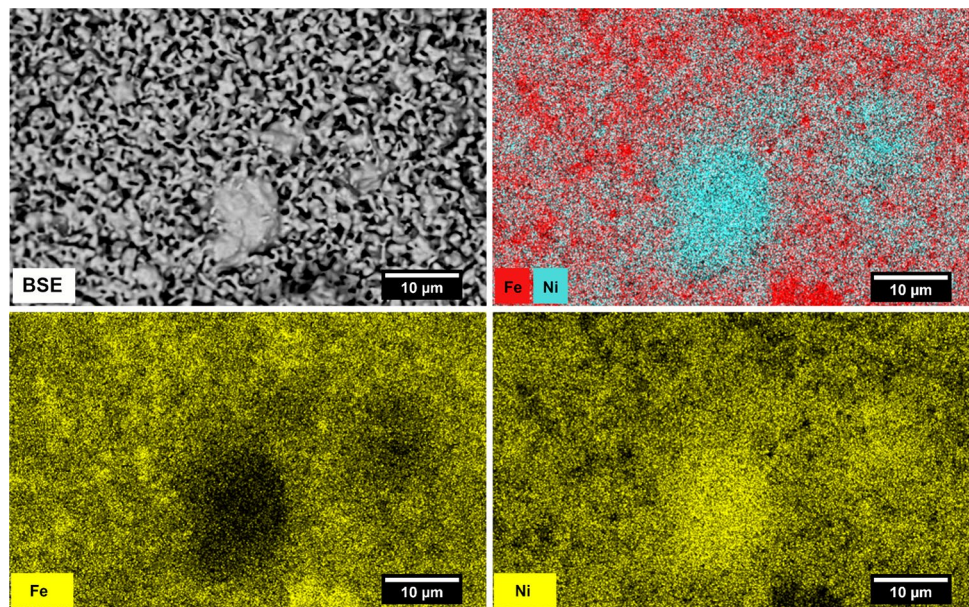


Table 4 Summary of energy-dispersive X-ray spectroscopy data for the FN1 and FN5 alloys

Alloy	Minimum	Maximum	Mean
FN1	57 ± 9	98 ± 9	86 ± 1
FN5	7 ± 9	46 ± 9	20 ± 1

All values are for iron in wt%. The residue is nickel

- The alloys form with no release of carbon dioxide or greenhouse gases, assuming that the electricity required to heat the sample is from carbon-free sources.
- This has the potential to greatly reduce greenhouse gas emissions from metals industries associated with secondary metallurgical processes. With appropriate supporting technologies, such as electricity supply and refractory production, the process can conceivably become entirely carbon-free.

To develop this concept further, the trials must first be scaled up toward an industrially relevant scale. In these scaled up trials, oxygen content will be accurately identified and measured using combustion analysis, and the kinetics and thermodynamics of the reduction process will be studied at each level of upscaling. It must also be proven that it is possible to form materials that are homogeneous on microscopic and mesoscopic scales. The trials must be extended to more alloy systems and higher-order mixtures. Hydrogen reduction trials involving raw materials that are widely available, including both real ores and waste products such as slag, mill scale, and flue gas dust will also be carried out in future to obtain valuable metals. A techno-economic assessment and an assessment of the impact on sustainable development of the method must be performed to motivate and justify its development.

Acknowledgements The authors at KTH gratefully acknowledge financial support from the Swedish Energy Agency under project number 49836-1 within the Industriklivet program.

Funding Open access funding provided by Royal Institute of Technology. Funding was provided by Energimyndigheten (Grant No. 49836-1).

Declarations

Conflict of interests The authors declare that they have no conflict of interest.

Open Access This article is licensed under a Creative Commons Attribution 4.0 International License, which permits use, sharing, adaptation, distribution and reproduction in any medium or format, as long as you give appropriate credit to the original author(s) and the source, provide a link to the Creative Commons licence, and indicate if changes were made. The images or other third party material in this article are included in the article's Creative Commons licence, unless indicated otherwise in a credit line to the material. If material is not included in the article's Creative Commons licence and your intended use is not permitted by statutory regulation or exceeds the permitted use, you will need to obtain permission directly from the copyright holder. To view a copy of this licence, visit <http://creativecommons.org/licenses/by/4.0/>.

References

- IEA (2020) Iron and steel technology roadmap. Paris
- Joint Research Centre (2022) EU climate targets: how to decarbonise the steel industry. In: EU science hub. https://joint-research-centre.ec.europa.eu/jrc-news-and-updates/eu-climate-targets-how-decarbonise-steel-industry-2022-06-15_en#_ftn1. Accessed 1 Sep 2023
- Oxford Economics (2019) The role of manufacturing in the global economy
- Suopajarvi H, Kemppainen A, Haapakangas J, Fabritius T (2017) Extensive review of the opportunities to use biomass-based fuels in iron and steelmaking processes. *J Clean Prod* 148:709–734. <https://doi.org/10.1016/j.jclepro.2017.02.029>
- World Steel Association (2022) Hydrogen (H₂)-based ironmaking
- Polyakov O (2013) Technology of ferronickel. Handbook of ferroalloys: theory and technology. Elsevier, Amsterdam, pp 367–375
- Tilliander U, Aune RE, Seetharaman S (2022) Kinetics studies of hydrogen reduction of Cu₂O. *Int J Mater Res* 97:72–78. <https://doi.org/10.1515/ijmr-2006-0011>
- Wenjing W (2021) Assessment of raw materials in stainless steelmaking—their energy consumption and greenhouse gas emission. KTH Royal Institute of Technology Thesis, Stockholm
- European Commission, Directorate-General for Internal Market, Industry, et al (2020) Critical raw materials resilience: charting a path towards greater security and sustainability. Brussels
- Burton J (2022) Geological survey: 2022 final list of critical minerals. U. S. Geological Survey
- Gille G, Bredthauer J, Gries B et al (2000) Advanced and new grades of WC and binder powder—their properties and application. *Int J Refract Metals Hard Mater* 18:87–102. [https://doi.org/10.1016/S0263-4368\(00\)00002-0](https://doi.org/10.1016/S0263-4368(00)00002-0)
- Norgren S, García J, Blomqvist A, Yin L (2015) Trends in the P/M hard metal industry. *Int J Refract Metals Hard Mater* 48:31–45. <https://doi.org/10.1016/j.ijrmhm.2014.07.007>
- Koehler L, Koehler Associates (2015) Powder metallurgy nickel and nickel alloys. In: Samal P, Newkirk J (eds) ASM handbook, powder metallurgy. ASM International, pp 673–681
- Spreitzer D, Schenk J (2019) Reduction of iron oxides with hydrogen—a review. *Steel Res Int*. <https://doi.org/10.1002/srin.201901018>
- Buschow KHJ, Cahn RW, Flemings MC et al (2001) The encyclopedia of materials—science and technology. Pergamon Imprint
- Spreitzer D, Schenk J (2019) Iron ore reduction by hydrogen using a laboratory scale fluidized bed reactor: kinetic investigation—experimental setup and method for determination. *Metall Mater Trans B* 50:2471–2484. <https://doi.org/10.1007/s11663-019-01650-9>
- Fedorov AV, Kukushkin RG, Yeletsky PM et al (2020) Temperature-programmed reduction of model CuO, NiO and mixed CuO–NiO catalysts with hydrogen. *J Alloys Compd*. <https://doi.org/10.1016/j.jallcom.2020.156135>
- Cortez OA, Moura FJ, de Albuquerque BE et al (2014) Fe–Ni alloy synthesis based on nitrates thermal decomposition followed by H₂ reduction. *Metall Mater Trans B* 45:2033–2039. <https://doi.org/10.1007/s11663-014-0221-x>
- De Graaf JE (1979) The treatment of lateritic nickel ores—a further study of the Caron process and other possible improvements—part 1. Effect of reduction conditions. *Hydrometallurgy* 5:47–65. [https://doi.org/10.1016/0304-386X\(79\)90027-6](https://doi.org/10.1016/0304-386X(79)90027-6)
- Hui TX, Zao LR, Yao L et al (2014) Ferronickel enrichment by fine particle reduction and magnetic separation from nickel laterite ore. *Int J Miner Metall Mater* 21:955–961. <https://doi.org/10.1007/s12613-014-0995-5>
- Elliott R, Pickles CA (2017) Thermodynamic analysis of the selective reduction of a nickeliferous limonitic laterite ore by hydrogen. *High Temp Mater Processes* 36:835–846. <https://doi.org/10.1515/htmp-2015-0208>
- Forbes C, Evans M, Hastings N, Peacock B (2010) Cauchy distribution. *Statistical distributions*. Wiley, Hoboken, pp 66–68
- Okamoto H, Schlesinger ME, Mueller EM (2016) Cu–Ni (Copper–Nickel). ASM handbook—alloy phase diagrams. ASM International, p 313
- Khort A, Roslyakov S, Loginov P (2021) Solution combustion synthesis of single-phase bimetallic nanomaterials. *Nano-Struct Nano-Objects* 26:1–5. <https://doi.org/10.1016/j.nanoso.2021.100727>
- Voronin VI, Berger IF, Proskurnina NV, Goschitskii BN (2016) Defects in a lattice of pure nickel subjected to fast-neutron irradiation followed by annealings: neutron-diffraction examination. *Phys Met Metallogr* 117:348–354. <https://doi.org/10.1134/S0031918X16040141>
- Ng SC, Brockhouse BN, Hallman ED (1967) Characterization of large alloy single crystals by neutron diffraction. *Mat Res Bull* 2:69–73. [https://doi.org/10.1016/0025-5408\(67\)90044-X](https://doi.org/10.1016/0025-5408(67)90044-X)
- German RM (1994) Powder metallurgy science. Metal Powder Industries Federation, Princeton, pp 92–96
- Samal P, Newkirk J (2015) Chemical and electrolytic methods of powder production. ASM handbook, volume 07—powder metallurgy. ASM International, p 72
- Hessels CJM, Smeets AHJ, Finotello G et al (2023) Sintering behavior of combusted iron powder in a packed bed reactor with nitrogen and hydrogen. *Particuology* 83:8–17. <https://doi.org/10.1016/j.partic.2023.02.007>
- Okamoto H, Schlesinger ME, Mueller EM (2016) Fe–Ni (Iron–Nickel). ASM handbook—alloy phase diagrams. ASM International, p 347

Publisher's Note Springer Nature remains neutral with regard to jurisdictional claims in published maps and institutional affiliations.

Authors and Affiliations

Arun Kamalasekaran¹  · Pelle Mellin² · Christopher Hulme¹

✉ Arun Kamalasekaran
arunka@kth.se

² Swerim AB, Isafjordsgatan 28A, 164 40 Kista, Sweden

¹ Department of Materials Science and Engineering,
KTH Royal Institute of Technology, Brinellvägen 23,
100 44 Stockholm, Sweden